Title

Mammary tumor-derived transplants as breast cancer models to evaluate tumor-immune interactions and therapeutic responses

Journal

Cancer Research, 82(3)

ISSN

0008-5472

Authors

Moore, Jade
Ma, Lin
Lazar, Ann A
et al.

Publication Date

2022-02-01

DOI

10.1158/0008-5472.can-21-0253

Peer reviewed

Mammary tumor-derived transplants as breast cancer models to evaluate tumor-immune interactions and therapeutic responses

Jade Moore, Ph.D.[1], Lin Ma, Ph.D.[1,5], Ann A. Lazar, Ph.D.[2,3], Mary Helen Barcellos-Hoff, Ph.D.[1,4]

[1] Department of Radiation Oncology and Helen Diller Family Comprehensive Cancer Center, University of California, San Francisco, CA 94158, California, USA
[2] Department of Oral Epidemiology, School of Dentistry, University of California San Francisco, San Francisco, California
[3] Department of Epidemiology and Biostatistics, University of California San Francisco School of Medicine, San Francisco, California
[4] Correspondence to maryhelen.barcellos-hoff@ucsf.edu
[5] Current address: Department of Stomatology, Shenzhen University General Hospital, Shenzhen, China 518055.

Keywords: Breast cancer; patient-derived transplants; immune cells; mouse models

Running title: Mammary tumor-derived transplants

Financial support: This research was supported by USC-3, an imCORE Network project funded by Genentech Inc., and the National Institutes of Health grants R01CA190980, R01CA239235 and T32CA108462.

Corresponding Author
Mary Helen Barcellos-Hoff, Ph.D.
Department of Radiation Oncology
Helen Diller Family Comprehensive Cancer Center
School of Medicine
University of California, San Francisco
2340 Sutter St., San Francisco, CA 94143
(415) 476-8091
MaryHelen.Barcellos-Hoff@ucsf.edu
ORCHID ID 0000-0002-5994-9558

Conflicts of interest/Competing interests: MHBH has or is a recipient of research grants paid to UCSF from Genentech imCORE related to this publication; she also has received funding, Varian, Inc. and Lilly, Inc. and consultation fees from EMD-Serono, Varian, and Genentech for work unrelated to this publication. JM, LM and AL report no conflicts of interest.

Moore, J., Ma, L., Lazar, A. A., & Barcellos-Hoff, M. H. (2022). Mammary Tumor-Derived Transplants as Breast Cancer Models to Evaluate Tumor-Immune Interactions and Therapeutic Responses. Cancer Res, 82(3), 365-376. doi:10.1158/0008-5472.can-21-0253

Abbreviations: tumor microenvironment, TME; triple-negative breast cancer, TNBC; transforming growth factor beta, TGFβ; tumor infiltrating lymphocytes, TIL; estrogen receptor, ER; progesterone receptor, PR; human epidermal growth factor receptor 2, HER2; mammary tumor-derived transplant, mTDT; programmed death ligand 1, PD-L1;

Availability of data and material: Materials available upon request to corresponding author, MHBH. Gene expression data are archived in gene expression omnibus (GEO, RRID: SCR_005012) under accession number GSE152403.

Abstract

In breast cancer, the type and distribution of infiltrating immune cells are associated with clinical outcome. Moreover, cancers with abundant tumor infiltrating lymphocytes (TIL) are more likely to respond to immunotherapy, while those in which CD8+ T cells are completely absent (deserts) or excluded are less likely to respond. Detailed understanding of this biology is limited by a lack of preclinical breast cancer models that recapitulate TIL distributions and their associated biology. Here we established mammary tumor-derived transplants (mTDT) from 12 Trp53 null mammary tumors in syngeneic BALB/cJ mice and examined the stability of their growth rate, TIL distribution, and transcriptomic profiles. All mTDT were estrogen receptor negative. Half of the parental tumors were classified as infiltrated, and the rest were divided between excluded and desert phenotypes. After two orthotopic passages, most (70%) mTDT from infiltrated parents recapitulated this pattern, whereas the desert or excluded parental patterns were maintained in about half of daughter mTDT. Approximately 30% of mTDT gave rise to lung or liver metastases, although metastasis was not associated with a TIL phenotype. Unsupervised transcriptomic analysis clustered mTDT according to their TIL spatial patterns. Infiltrated mTDT transplanted subcutaneously and orthotopically were resistant to anti-PD-L1. Profiling implicated prolonged antigen stimulation and loss of effector function of lymphocytes rather than T cell exhaustion in the lack of response of infiltrated mTDT to checkpoint blockade. In summary, the molecular diversity and immune complexity of mTDT can facilitate the dissection of mechanisms of breast cancer response to immunotherapies.

Statement of Significance

A set of diverse preclinical models of breast cancer is characterized to enable mechanistic dissection of tumor-immune interactions and improve the efficacy of immunotherapies.

INTRODUCTION

Breast cancer is a heterogenous disease. Marker based classification of breast cancer uses amplification of human epidermal growth factor receptor 2 (HER2+) and expression of estrogen receptor (ER) and progesterone receptor (PR), those that lack all three are deemed triple-negative breast cancers (TNBC); each has prognostic significance. Breast cancer also generally shows an immune system dysfunction consisting of an inflammatory response favoring Th2 response, low frequency of infiltrating CD4+ and CD8+ T lymphocytes, and a tumor microenvironment (TME) characterized by abundant immune suppressive regulatory T and myeloid-derived suppressor cells (reviewed in (1)). Immune contexture (i.e., type of immune cells present and their specific location) is associated with clinical outcome in breast cancer (2-4). The pattern of tumor infiltrating lymphocytes (TIL) in human cancers is associated with the likelihood of response to immune checkpoint inhibitor immunotherapy (5,6). Infiltrated tumors characterized by a brisk, active lymphoctyic cell infiltrate are more likely to be responsive, while those devoid of lymphocytes, so-called deserts, or those in which TIL are excluded are less likely to respond. There is a significant correlation between TIL at diagnosis and overall survival in both TNBC and HER2+ breast cancer (7). Nonetheless, the response rate of TNBC to single agent checkpoint inhibition using antibodies to programmed cell death protein 1 (PD-1) or its ligand (PD-L1) is less than 10% (4,8-10). Thus, there is a pressing need to better understand how breast tumor cells interact with the immune cells in the TME.

Preclinical models are essential to every aspect of translational cancer research, from understanding the biology of the disease to developing new treatments. The National Cancer Institute (NCI)-60 cancer cell line panel represents the best characterized and most frequently used collection of human cancer models developed for in vitro drug development and screening (11). Xenografts established by growing these cell lines in immunodeficient mice are often used for preclinical studies, yet cell line derived tumor xenografts have limited power to predict clinical treatment outcomes (12). Patient-derived tumor xenografts that maintain the cell morphology and molecular signatures of the original patient tumor were developed to provide an additional translational model that better mirror the biology of human cancer patients (13,14). Even though patient biopsies are difficult to obtain and breast tumors have a low take rate (~20%) in mice (15), more than 500 breast cancer patient-derived xenografts representing all three clinical subtypes of breast cancer (i.e., 56% TNBC, 36% ER+, 8% HER2+) have been characterized for genomic, transcriptomic, and proteomic features, metastatic behavior and treatment response (13). These patient-derived breast cancer xenografts reflect the heterogeneity of disease, but the necessity of implantation in mice lacking functional immune system precludes studies of the contribution of the immune system to tumor heterogeneity or response to many immunotherapies. In contrast, carcinogen-induced and genetically-engineered mouse models provide the opportunity to study mechanisms of immune escape during carcinogenesis or response to immunotherapy in an immunocompetent setting (16).

The *Trp53* null mammary chimera syngeneic mouse model introduced by Jerry and Medina is widely used to study breast carcinogenesis (17). *Trp53* mammary epithelial transplants undergo normal ductal morphogenesis but progress from outgrowths to ductal carcinoma in situ to invasive carcinomas over the course of the animal's lifespan. The resulting cancers are markedly heterogenous with regard to molecular profiles, expression of hormone receptors, and histology (17-20), the spectrum of which recapitulate the diversity of human breast cancers (21,22). We recently showed that *Trp53 null* mammary tumors also exhibit distinct spatial TIL patterns (23), similar to those broadly described in human cancer (3). *Trp53* null mammary cancers can be classified as those in which lymphocytes are distributed (infiltrated), those lacking lymphocytes (desert), or ones in which lymphocytes are present at the tumor border (excluded). Here, we established mammary tumor-derived transplants (mTDT) to further exploit the molecular

diversity and immune complexity of the immunocompetent *Trp53 null* mammary model and characterized the stability of parent phenotypes to that of daughters. The diversity of mTDT characteristics in these families enable mechanistic dissection of cancer and immune cell interactions in the TME and detailed investigations of the contribution of these to therapeutic response.

MATERIALS and METHODS

Animals

All animal experiments were performed at the University of California, San Francisco (UCSF, San Francisco, CA). The protocols for animal husbandry and experiments were conducted with approval from the institutional review board. Six-to-eight-week-old *Foxn1^{nu}/ Foxn1^{nu}* outbred athymic nude from Taconic Laboratory (Albany, NY) and 8-week-old female BALB/cJ *Mus musculus* (RRID: IMSR_JAX:000651) from Jackson Laboratory (Sacramento, CA) were housed 5 per cage, fed with Lab diet #5001 Rodent Formula (Purina Animal Nutrition LLC), and provided water *ad libitum.*

Mammary tumor-derived transplants (mTDT)

Vials of viably frozen fragments from a bank of *Trp53* null tumors that were generated in prior experiments using *Trp53* null mammary chimeras in BALB/cJ mice (22,24,25) were chosen at random, thawed, and transplanted subcutaneously in outbred athymic Foxn1^{nu} homozygous nude mice. Mice were monitored by palpation twice weekly until the tumor reached ~0.5 cm^3. The tumor was resected and dissected into 4 portions in which one portion was cut into 1 mm^3 fragments for viable preservation in DMEM (Gibco, #10564-011) with 10% fetal bovine serum (Hyclone, #SH3007103) and 10% dimethyl sulfoxide (Sigma, #D2650) and stored in liquid nitrogen, one portion was frozen in liquid nitrogen for RNA and DNA extraction, one portion was embedded in optimum cutting temperature compound (OCT) for cryosectioning, and one portion was formalin-fixed and paraffin embedded (FFPE) by UCSF pathology core. This expanded tumor was termed F1. F1 fragments were transplanted bilaterally in the inguinal mammary fat pad or subcutaneously, as indicated, in syngeneic BALB/cJ mice. Tumor growth was monitored by palpation or caliper measurement twice weekly and harvested when the tumor reached ~0.5 cm^3. Tumor volume was calculated as $V = (W^2 \times L) / 2$ for each measurement. These F2 tumors were resected into four portions in the same manner as F1 tumors. Sequential transplantation from this stock were numbered F3. The characterization experiments described herein were carried out with 12 parental tumors, alphabetically designated A-L, and their F2 and F3 mTDT.

To determine mTDT metastatic potential, 8-10-week-old mice were transplanted orthotopically and tumor growth was monitored by caliper measurement twice weekly. mTDT were resected upon reaching ~0.5 cm^3. Mice were monitored by palpation for tumor recurrence and by observation for labored breathing, poor grooming, or loss of 15% body weight, which were the predetermined basis for termination. All other mice were sacrificed at 1-month post-tumor resection. The lung and liver of mice in which tumors were resected were visually inspected for gross nodules indicative of metastases.

For experiments using anti-programmed death-ligand 1 (PD-L1; Roche PD-L1 9708, 6E11), 8-10-week-old mice were transplanted subcutaneously or orthotopically with F2 mTDT from six families. Mice with established tumors, 130-230 mm^3, were randomized into control (irrelevant IgG) or anti-PD-L1 treatment groups. Antibody was administered intraperitoneally twice weekly until tumor burden exceeded 1 cm^3 or mice lost 15% of body weight. Initial treatment was 10 mg/kg followed by 5 mg/kg twice per week for up to 3 cycles total. Tumors were measured with calipers and mice were weighed three times weekly. Upon termination, the tumor was resected, weighed, and preserved as indicated.

Immunofluorescence

FFPE sections were dewaxed and rehydrated before using antigen unmasking solution (Vector Laboratories, #H-3300) according to the manufacturer's instructions, washed once with PBS (Thermo Fisher Scientific cat#10010023) and blocked with the supernatant of 0.5% casein (Spectrum, #CA205) in PBS stirred for 1 hour at room temperature. Slides were incubated overnight at 4°C with 100 µL primary antibody against the indicated antigen diluted in blocking buffer (0.5% casein in PBS) as indicated: anti-CD8 (Abcam Cat#ab4055, RRID: AB_304247, 1:200) and CD3e monoclonal antibody (SP7) (Thermo Fisher Scientific Cat#MA5-14524, RRID: AB_10982026, 1:100). After washing with 0.1% Tween 20 (Sigma-Aldrich Cat#P9416) in PBS, slides were incubated for 1 hour at room temperature with 100 µL fluorochrome-conjugated secondary antibody diluted 1:200 in blocking buffer (0.5% casein supernatant in PBS) of Alexa Fluoro-555-conjugated goat anti-rabbit (Thermo Fisher Scientific Cat#A27039, RRID: AB_2536100) for recognizing CD3e; Alexa Fluor 488 Donkey anti-Rat IgG (H+L) highly cross-adsorbed secondary antibody (Thermo Fisher Scientific Cat#A-21208, RRID: AB_2535794) for recognizing CD8. Nuclei were counterstained with 4', 6-diamidino-2-phenylindole (DAPI) (Molecular Probes Cat#D1306, 2 mg/mL). Sections were washed in PBS before mounting with VectaShield mounting medium (Vector Labs Cat#H-1000)

OPAL Multiplex

Multiplexed immunofluorescence staining was performed manually using Opal 6 color kit (NEL796001KT; PerkinElmer, Waltham, MA), which uses individual tyramide signal amplification (TSA)-conjugated fluorophores to detect various targets within an assay (26). FFPE sections were dewaxed with xylene 2 x 10 min and rehydrated through a graded series of ethanol solutions (100%, 90%, 70%) 1 x 5 min and H_2O 1 x 5 min and placed in a glass container filled with antigen retrieval (AR) buffer in Tris-EDTA (Vector Laboratories, #H-3301) according to the manufacturer's instructions. The slides were microwaved to bring the liquid to 100°C (9 min) and then microwaved an additional 10 min at 95°C. Slides were allowed to cool in the AR buffer for 20-30 min at room temperature and were then rinsed with deionized water and 1 X TN buffer (0.1 M Tris-HCl, pH 7.5; 0.15 M NaCl) (Invitrogen Cat#15567027). To initiate protein stabilization and background reduction, slides were incubated for 1 hour in blocking buffer (supernatant of 0.5% casein stirred for 1 hr in TN buffer) at room temperature in a humidified chamber. Slides were then incubated overnight at 4°C with primary antibodies as follows: CD3e monoclonal antibody (SP7) (Thermo Fisher Scientific Cat#MA5-14524, RRID: AB_10982026, 1:100), anti-CD8 (Abcam Cat# ab4055, RRID:AB_304247, 1:100), CD11b (M1/70) (Biolegend Cat#101201, RRID: AB_312784, 1:100), purified anti-mouse CD45 (30-F11) (Biolegend Cat#103101, RRID: AB_312966, 1:100), pSMAD2 (Cell Signaling Cat#3122S, RRID: AB_823638, 1:50), F4-80 monoclonal antibody (SP115) (Thermo Fisher Scientific Cat#MA5-16363, RRID: AB_2537882, 1:100), anti-wide spectrum cytokeratin antibody (abcam Cat#ab9377, RRID: AB_307222, 1:200) and recombinant anti-PD-L1 antibody (EPR20529) (Abcam Cat#ab213480, RRID: AB_2773715, 1:50). Endogenous peroxidase was quenched with fresh 3% H_2O_2 (Sigma-Aldrich Cat#H1009) in TN buffer for 10 min at room temperature then washed 1 X TN buffer for 5 mins with agitation. The slides were incubated at room temperature for 1 hour with anti-rabbit (Thermo Fisher Scientific Cat#31466, AB_10960844) or anti-rat (Thermo Fisher Scientific Cat#31470, RRID: AB_228356) in secondary antibody working solution (1:200) followed by 3 X 5 min wash with 0.05% Tween 20 (Sigma-Aldrich Cat#P9416) in TN buffer (TNT buffer). The slides were then incubated at room temperature for 10 min with one of the following Alexa Fluor tyramides (PerkinElmer) included in the Opal 6 kit to detect antibody staining (dilution 1:100), prepared according to the manufacturer's instructions: Opal 520, Opal 540, Opal 570, Opal 620 and Opal 690. After three additional washes with TNT buffer, the nuclei were counterstained with DAPI (Molecular Probes Cat#D1306, 1:200) for 10 min and mounted with Vectashield Hard Set (Vector Labs Cat#H-1400, Burlingame, CA). Spleen, lung, or C19 tumor tissues with and without primary antibody and/or

omitting the fluor tyramides were used for positive and negative controls. Once each target was optimized in uniplex slides, the Opal 6 multiplexed assay was performed consecutively by using the same steps as those used in standard immunofluorescence and the detection for each marker was completed before application of the next antibody. The best sequence of antibodies for multiplex staining was determined for each combination: panel 1 (CD3, CD8, CD11b, CD45 and DAPI) and panel 2 (CD8, pSmad2, PD-L1, F4-80, pan-cytokeratin and DAPI).

Image collection and analysis

CD3/CD8 immunofluorescence was imaged with a 20X Zeiss Plan-Apochromat objective with 0.95 numerical aperture on Zeiss Axiovert epifluorescent microscope equipped with a CCD Hamamatsu Photonics monochrome camera with a 1392 x 1040-pixel size at 12 bits per pixel depth. All images were assembled as false-color images using the ZEN 2.3 imaging software (Zeiss). The quantitative immune infiltrate status was determined in FFPE sections in which nuclei were counterstained with DAPI, and CD8 lymphocytes were localized by ZEN intellesis™ software (Zeiss). The pattern of lymphocyte distribution of parent tumors was determined by 2 observers blind to the origin of the mTDT. In the instance of disagreements, a third observer blind to the origin resolved the discrepancies. For mTDT, 3-5 images were taken of both the center and edge of each tumor and the following scoring was used to assign lymphocyte distribution: infiltrated were defined as >5 CD8+ T cells interior/high powered field (HPF), excluded were defined as >5 cells/HPV on edge and <3 CD8+ T/HPF cells interior, and deserts were defined as <3 CD8+ T cells/HPF interior or edge.

OPAL-stained slides were imaged using the Vectra 2.0 multispectral imaging system (PerkinElmer) using the fluorescence protocol at 10 nm λ from 420 nm to 720 nm. Single stained slides for each marker and associated fluorophore were used to establish the spectral library. After low magnification scanning at 10X, the specimens were scanned using the Phenochart 1.0.4 (PerkinElmer) viewer at high resolution (20X). The data from the multispectral imagin were analyzed by inForm 2.1 imaging software (PerkinElmer). Immune cell populations from each panel were quantified from 5 to 7 high powered fields that were randomly chosen and imaged at 20X. Pan-cytokeratin marker was used to distinguish tumor versus stroma. Using inForm™ software, inForm tissue finder tool was trained by drawing over areas of each tissue type to classify tumor versus stroma. The individual markers from each multiplex panel were quantified using the trainable tissue segmentation and phenotype algorithm that identified positive cells in the tumor and stromal regions based on the mean fluorescent intensity per case. The percent positive cells per marker was divided by the tumor or stroma area to obtain average density of cells per compartment.

Gene expression profiling

For NanoString®, frozen tumor (20 mg) was lysed in 1 mL TRIzol reagent (Invitrogen Cat#15596018) and homogenized with Omni Tissue Homogenizer on medium setting for 30 seconds then incubated 3 minutes in 0.2 mL chloroform followed by centrifuging for 15 minutes at 12,000 x *g* at 4°C. The aqueous phase was transferred to a new tube and 0.5 mL isopropanol was added for 10 minutes. Samples were then centrifuged for 10 minutes at 12,000 x *g* at 4°C. The supernatant was discarded, and the white gel-like pellets were resuspended in 1 mL of 75% ethanol. The samples were then vortexed briefly, then centrifuged for 5 minutes at 7,500 x *g* at 4°C. The supernatant was discarded and the RNA pellet airdried for 10 minutes before resuspending in 30 µL of RNase-free water. The samples were incubated in a heat block at 60°C for 15 minutes before determining total RNA quality (RIN > 7.0) and quantity was determined using an Agilent 2100 Bioanalyzer and Nanodrop ND-100. 100 ng RNA were successfully hybridized to the NanoString® PanCancer IO360 Panel code set, according to the recommendations of the manufacturer (NanoString Technologies, Inc., Seattle, Washington,

USA). The expression of 750 immune-related genes and 20 housekeeping genes were assessed. The nSolver 2.6 software was used to normalize expression values using housekeeping genes following the manufacturer's recommendations. Gene clustering was done using Pearson correlation coefficient (PCC). For evaluation of a chronic TGFβ-induced gene signature (27), normalized gene expression was averaged across the gene signature. All heatmaps were generated using ggplot2 package (RRID: SCR_014601) available through R.

For bulk RNA sequencing, fragments (~50 mg) of liquid nitrogen preserved mTDT (n=66) were shipped on dry ice to Q^2 Solutions | EA Genomics for isolation of total RNA using proprietary methods. The amount and quality of specimens was assessed using Agilent Bioanalyzer and NanoDrop analysis. Total RNA samples that met quality control metrics were enriched for mRNA, fragmented and converted into indexed cDNA libraries for Illumina sequencing. Generated cDNA libraries were quantified by qPCR using primers specific for Illumina sequencing adapters using TruSeq stranded mRNA at 30 M 50 bp PE assay. Raw sequencing data were received in fastq format and read mapping was performed using Rsubread package (RRID: SCR_016945) against *Mus musculus* GRCm38 and human GRCh38 genome (28). Gene expression data are archived in gene expression omnibus (GEO, RRID: SCR_005012) under accession number GSE152403.

Statistical analysis

Descriptive statistics were used to summarize the data, with frequencies and counts for categorical variables, and means, standard deviations, medians and inter-quartile range (IQR) for data measured on a continuum. Chi-square or Fishers exact test were used to compare categorical variables, and for continuous variables Mann-Whitney test, as indicated. Tumor volume data was not normally distributed and were therefore log transformed for all analyses. To assess whether tumor volume trajectories differed by infiltrate status for the F2 and F3 generation, we used a separate linear mixed effects regression model (29). We flexibly modeled trajectories by testing whether including quadratic or cubic terms for time or random slopes for each mouse improved the model fit and included them if indicated by a significant *(P* < 0.05) likelihood ratio test. In both F2 and F3 models, random intercepts and slopes improved the model fit as did fixed intercepts and slopes for each infiltrate. We estimated whether trajectories changed over time or differed by infiltrate status via a post-estimation F-test using the contrast statement in SAS proc mixed to assess any overall differences across infiltrate. We also accounted for clustering of families in the mixed model using a separate random effect. Kenward-Rogers denominator degrees of freedom were used. The benefit of the mixed-effects models is that they produce unbiased estimates even when some mice have missing observations, accommodate irregular time measurement and account for clustering by families and mice, as required in our data. Overall survival was defined as time from date of tumor to mouse sacrifice date (*survival* package) and hazard ratios (HRs) and associated 95% confidence intervals (CIs) were computed using multivariable Cox regression (*survfit* package) analyses adjusted for site, growth rate, family, and size of tumor at start of treatment. Proportional hazards assumption was met, and it was checked via an interaction term between each variable and log of time. Two-sided p-values less than 0.05 were considered statistically significant. The statistical analysis for all experimental data was performed using Prism 7 (GraphPad Prism, RRID: SCR_002798) and SAS v. 9.4 was used for all analyses.

RESULTS

Murine tumor-derived transplants (mTDT)

mTDT were established from a bank of viably frozen primary tumors generated from experiments using the *Trp53* null mammary chimera model (22,24,25). In this model, *Trp53* null mammary fragments were transplanted to inguinal fat pads of 3-week-old syngeneic BALB/cJ mice in which the endogenous epithelium was surgically ablated, so-called cleared fat pads (**Fig. 1A**). The

resulting *Trp53* null mammary chimeras undergo ductal outgrowth and most develop mammary tumors in the second year of life. These *Trp53* null tumors are diverse in regard to histology, growth rate, composition and genomics (19,20,23,24). Randomly chosen vials of viably frozen fragments of *Trp53 null* primary tumors, designated as F0, were thawed and the fragments were bilaterally transplanted subcutaneously in 8-week-old athymic nude mice. Each mouse that gave rise to one or two tumors were designated as F1. F1 tumors were resected upon reaching ~1 cm^3, diced into 1 mm^3 fragments (~150 fragments per tumor), viably frozen and stored in liquid nitrogen. Fragments of F1 tumors from 12 parental tumors named alphabetically, A-L, were orthotopically transplanted bilaterally into intact inguinal mammary glands of 8-10-week-old BALB/cJ mice, which were designated F2; F3 mTDT were similarly established from F2 tumors.

Orthotopic tumor take rate was 90% for both F2 (63/70) and F3 (54/60) mTDT. The tumor growth rate of F3 mTDT was significantly slower *(P* = 0.05, Mann-Whitney test) than F2 mTDT (**Fig. 1B**). Orthotopic transplantation into intact mammary fat pads is considered desirable for breast cancer patient-derived xenografts, as it most closely represents the human breast microenvironment (15), yet subcutaneous tumors are frequently used in preclinical models to facilitate evaluation of tumor growth. Hence, we compared F3 tumor engraftment and growth between orthotopic and subcutaneous transplantation in BALB/cJ mice. As a group (**Table 1B**), neither tumor take nor site-specific growth rate at orthotopic (77.5%, 31/40) and subcutaneous (80%, 32/40) sites were statistically significant different *(P* = 1.0, Chi-square test). The tumor growth rate of F2 mTDT was heterogenous **(Fig. 1C).** The successful mTDT transplantation at either subcutaneous or orthotopic sites provides model versatility for further investigation.

Parental and mTDT were histologically classified using hematoxylin and eosin and immunofluorescence to assess the frequency of ER and PR positive cells. Three histological patterns were evident (**Fig. 1D**): adenocarcinoma characterized by small “ducts”, spindle cell consisting of malignant cells with a distinct elongated phenotype, and undifferentiated composed of large irregular cells. The histology of respective parental tumors was preserved in F2 and F3 mTDT. Of the 12 parental tumors, one was ER and PR positive and 11 were ER and PR negative tumors. Neither F2 or F3 mTDT of the ER and PR positive parent (family B) maintained hormone receptors; thus, all mTDT studied were ER and PR negative.

Patterns of lymphocyte infiltrate across mTDT passage

Based on the spatial TIL distributions, human cancers are broadly categorized as infiltrated, deserts or excluded (30). *Trp53* null primary tumors also exhibit these TIL patterns (23). We used whole slide imaging of multiplex immunofluorescence to qualitatively categorize parental tumors as infiltrated, excluded, or desert (**Fig. 2A**). Half of the parental tumors (6/12) were classified as infiltrated, 25% (3/12) were excluded, and 25% (3/12) were deserts (**Fig. 2B**).

We next quantitatively classified mTDT immune cell infiltrate based on the frequency per HPF of CD8+ cytotoxic T cells at the tumor edge versus the center (**Fig. 2C**). The tumors assigned to the infiltrated category had more CD8+ T cells within the tumor than at the tumor edge while excluded tumors had more CD8+ T cells at the edge of tumors (**Fig. 2D**). Desert tumors were devoid of CD8+ T cells. Using this objective metric, the spectrum of immune infiltrate patterns of F2 mTDT resembled that of primary tumors: 57% were infiltrated (31/54), 32% excluded (17/54), and 11% deserts (6/54). The F3 mTDT similarly maintained the spectrum with 55% infiltrated (22/40), 27.5% excluded (11/40) and 17.5% deserts (7/40). However, the fidelity of mTDT to recapitulate the parental immune infiltrate phenotype was not uniform (**Fig. 2E**). The infiltrated parental phenotype was the most stable in that 72% of mTDT were classified as infiltrated across generations, whereas 20% were excluded and 8% were desert. The mTDT from excluded primary tumors were the least stable. The excluded parental tumors gave rise to 67% infiltrated and 33% excluded in F2, and 27% infiltrated, 55% excluded and 18% desert at F3. Desert parent tumors

gave rise to 25% infiltrated, 44% excluded and 31% desert F2 mTDT and 33% each immune infiltrate in F3 tumors. The tumor TIL pattern correlated with histology: 57% of infiltrated tumors were undifferentiated, 61% of excluded were adenocarcinoma, and deserts were distributed between 43% undifferentiated and 38% adenocarcinoma (P = 0.0001, Chi-square test). Spindle cell histology was exhibited by 20% of tumors with infiltrated, 10% excluded, and 19% of desert TIL phenotype.

Cancers arising from *Trp53-null* outgrowths after host irradiation are metastatic (22,24). We tested the metastatic potential of mTDT from 3 infiltrated, 2 excluded and 1 desert family. Of 29 mice, 9 (31%) developed gross lung and/or liver nodules indicative of metastases. Four were from mTDT of an infiltrated family, four were from excluded and one arose from a desert mTDT. All mTDT (n=4) from infiltrated family K (undifferentiated histology) gave rise to metastases while 50% (n=4) of excluded mTDT families J (undifferentiated) and D (adenocarcinoma) metastasized. This suggests that metastatic potential is related to family rather than TIL phenotype. In human breast cancer, certain molecular subtypes (i.e., HER2+ and TNBC) are associated with faster tumor growth rates (31). Previous studies in our lab found that the frequency of CD8+ TIL correlates with tumor growth rate of primary *Trp53* null tumors, in which slower growth was associated with greater density of lymphocytes, consistent with active, yet ineffective, cytotoxic T cells (23). We evaluated tumor growth as a function of immune infiltrate phenotype across generations. Tumor growth rate was not associated with immune infiltrate status in the F2 generation (**Fig. 2F**, P = 0.87), but F3 excluded mTDT grew significantly slower than infiltrated F2 mTDT (**Fig. 2G**, P = 0.04).

Characterization of mTDT from infiltrated families

Tumor engraftment and growth were comparable between orthotopic and subcutaneous transplantation, we next characterized the TME of mTDT based on location. We analyzed the distribution of stroma, PD-L1, phosphorylated SMAD2 (pSMAD) as evidence of TGFβ activity, and macrophage marker F4/80 as a function of mammary tumor location, i.e., orthotopic compared to subcutaneous, in infiltrated families (**Fig. 3A**). Components of the TME were affected by site in some families but this was not uniform. For example, the amount of stroma in family H mTDT was significantly greater (P < 0.0001) when grown in the subcutaneous site compared to orthotopic but family I mTDT showed the opposite effect, and the stromal component of family E and G mTDT were unaffected by site (**Fig. 3B**). CD8+ T cells were enriched in orthotopic mTDT from families E and G compared to subcutaneous tumors but were unaffected by site of implantation in mTDT from families H and I (**Fig. 3C**). Family I mTDT had significantly more PD-L1+ cells in subcutaneous tumors (**Fig. 3D,** P < 0.01) and family G mTDT had significantly more F4-80+ cells in orthotopic tumors (**Fig. 3E,** P < 0.0001). pSMAD2 varied by nearly 2-fold between families but did not significantly differ between mTDT implantation sites (**Fig. 3F**).

Although response to checkpoint inhibition monotherapy is rare in TNBC patients (4,8-10), it is associated with TIL density in other solid cancers. Thus, we anticipated that mTDT from infiltrated parents, which largely maintain infiltrate status, would respond to checkpoint inhibition. Cancer patients who respond to PD-L1 inhibition express PD-L1 on tumor-infiltrating immune cells (32,33). In contrast, the tumors of patients who have poor response are characterized by high expression of reactive stroma and TGFβ signaling that is associated with lower expression of immune markers (34). Macrophages play complex roles that can oppose immunotherapy (35). Given these factors, we tested mice bearing orthotopic or subcutaneous mTDT from 6 infiltrated families that were randomized into control (non-specific IgG; n=27) or anti-PD-L1 (clone 6E11; n=31) treatment groups. Regardless of tumor implantation site, tumor growth was not affected by anti-PD-L1 (**Fig. 3G**). Anti-PD-L1 treatment did not affect median overall survival (29 $\pm$ 9.8 vs 29 $\pm$ 9.9) analyzed by Kaplan-Meir survival (**Fig. 3H**). However, parental origin was associated with survival (**Fig. 3I**). A multivariable Cox regression analysis adjusted for site, growth rate,

family, and size of tumor at start of treatment indicated that overall survival was significantly associated with parental origin (hazard ratio (HR) 2.25 95% confidence intervals (CI) 1.51-3.35, p=0.00007) and tumor growth rate (HR 1.20, 95%CI (1.017-1.42, p=0.03) but not with size, orthotopic versus subcutaneous implantation or treatment.

Transcriptomics cluster tumors according to immune infiltrate phenotypes

We hypothesized that transcriptional programs associated with mTDT immune infiltrate pattern might inform their response to checkpoint blockade monotherapy. First, we determined how mTDT map to human breast intrinsic molecular subtypes using RNAseq data from primary tumors (n=9) and mTDT (n=57). Using PAM50 molecular subtyping, we assessed the distribution of intrinsic breast cancer subtypes. The overall subtype distribution in primary tumors was 45% basal (4/9), 11% HER2 (1/9), 22% luminal A (2/9), 11% luminal B (1/9) and 11% normal (1/9) (**Fig. 4A**). The PAM50 proportion in mTDT was 25% basal (14/57), 16% HER2 (9/57), 21% luminal A (12/57), 21% luminal B (12/57) and 17% normal (10/57). All mTDT were ER and PR negative, similar to TNBC that display heterogenous patterns of morphology, genetic, immunophenotypic and clinical features (36,37). The TNBC subtyping tool subdivides marker classified TNBC transcriptomes into basal-like 1 and 2, immunomodulatory, mesenchymal, mesenchymal stem-like, and luminal androgen receptor (38). Primary tumors were classified as 33% (3/9) mesenchymal, 33% (3/9) immunomodulatory, 11% (1/9) mesenchymal stem-like and 22% (2/9) unstable (**Fig. 4B**). No primary tumors were classified as basal-like. The TNBC subtype distribution was similar in the F2 generation: 23% (13/57) mesenchymal, 32% (18/57) immunomodulatory, 10% (6/57) mesenchymal stem-like and 18% (10/57) unstable. Basal-like (14%, 8/57) and luminal androgen receptor (3%, 2/57) subtype were also present in the F2 mTDT. A third of primary and F2 were subtyped as immunomodulatory, which is considered a characteristic of the tumor rather than the immune cell infiltrate (39).

To investigate the transcriptional programs associated with mTDT immune infiltrate pattern that might explain the lack of response to checkpoint blockade monotherapy, we used the NanoString PanCancer IO 360™ gene expression panel that consists of 770 genes involved in the interplay between cancer cells, TME and immune cells (40) to analyze 5 primary tumors and 19 mTDT representing all infiltrate phenotypes. Unsupervised hierarchical clustering of all genes identified 2 major clades distinguished by 5 major gene clusters (**Fig. 4C**). F0 tumors clustered together in the left most dendrogram arm, regardless of lymphocyte infiltrate, whereas mTDT replicates from one parent clustered together, which suggests coherence of transcriptional programs. A subcluster of the left clade consisted of most (12/13) infiltrated mTDT whereas mTDT classified as desert (4/6) or excluded (3/5) clustered in the right most clade of the dendrogram.

The 5 gene clusters represent genes associated with lymphocyte activation, cytokine mediated signaling. and cell proliferation and activation. Interestingly, infiltrated tumors in the left arm of the dendrogram were characterized by weak lymphocyte activation, indicated by *Cd40lg, Zap70, Prf1, Lck* and *Lag3* in gene cluster 1 and 2, and strong cytokine mediated signaling as exemplified by *Tgfb1* in cluster 3 and *Il1b1* and *Il6R* in cluster 4. In comparison, desert and excluded tumors in the right dendrogram arm were characterized by relatively greater lymphocyte activation and cytokine mediated signaling. In gene clade 5, expression of genes *Egfr, Fgfr1* associated with cell proliferation and *Atm, Brca1, Ccne1* involved in DNA repair were increased in desert and excluded tumors compared to infiltrated tumors. A pair of excluded tumors and a desert were distinguished by high expression of 9 E-cadherin gene targets (*Kif2c*, *Id4, Epcam, Pkp3, Jag2, Lamc2, Sfrp1, Col17a, Lama1*) at the bottom of gene clade 5.

Next, we tested whether the molecular diversity and immune complexity of *Trp53* null mTDT facilitate dissection of mechanisms regulating lymphocytic infiltrate. Transforming growth factor β (TGFβ) is a key TME component that can elicit immunosuppressive phenotypes in immune cells,

including dendritic cells, tumor-associated macrophages, regulatory T cells and cytotoxic T cells, as well as fibroblasts (34,41), and is autocrine survival signal for myeloid precursors that drives their differentiation to highly immunosuppressive myeloid derived suppressor cells at the expense of macrophages and dendritic cells (42). We previously identified a 50-gene signature of chronic TGFβ signaling using human breast epithelial MCF10A cell line treated for a week with TGFβ (27). Average gene expression of 8 genes represented in Nanostring IO360 panel was used to conduct supervised hierarchical clustering of mTDT. High TGFβ signaling was associated with mTDT with excluded phenotypes while low TGFβ was predominantly associated with the desert phenotype (**Fig. 4D**). This stratification is consistent with reported association of TGFβ and lymphocytic exclusion in bladder cancers of patients who did not respond to checkpoint inhibition (34).

We used NanoString mouse immune exhaustion signature to ask if exhausted T cells are associated with lack of response to anti-PD-L1 monotherapy. T cell exhaustion is a state of dysfunction in a chronic environment and characterized by high levels of inhibitory receptors such as lymphocyte activation gene 3 protein (*Lag3*), T cell immunoglobulin, immunoreceptor tyrosine-based inhibitory motif domain (*Tigit*), cytotoxic T lymphocyte antigen-4 (*Ctla4*) (43). Of the 30 genes from the T cell exhaustion panel, 18 were present in the PanCancer IO360 panel, which were used to performed supervised hierarchical clustering of infiltrated tumors. We identified 2 major gene dendrogram arms (**Fig. 4E**). In the lower arm of gene dendrogram, T cell inhibitory receptors gene expression, *Tigit* and *Ctla4* were relatively low across most infiltrated tumors but *Lag3* expression was relatively high in most infiltrated tumors suggesting potential loss of T cell cytotoxic function. However, in the upper arm of the dendrogram, *Casp3* gene expression is pronounced, suggesting either activation of T cells or deletion of expanded effector T cells. These data suggest prolonged antigen stimulation of lymphocytes in infiltrated tumors and loss of effector function.

Together these data show that the mTDT model recapitulates the complex interactions among cancer cells, TME and infiltrating immune cells that together form barriers to effective immunotherapy.

DISCUSSION

Clearly a major challenge to implementing effective immunotherapy for breast cancer lies in our limited mechanistic understanding of critical components of the TME intertwined with the diversity of intrinsic molecular subtypes. mTDT described herein recapitulate the variety of TME components and immunosuppressive signals in human breast cancer, which addresses a gap in current preclinical breast cancer models. In particular, mTDT represent biological diversity pertinent to studying immunotherapy responses. Most mTDT recapitulate their parental patterns of T cell distribution, infiltrated, excluded, and desert. The infiltrated phenotype was the most stable, wherease the excluded tumors were the least stable; in some cases, they gave rise to only infiltrated mTDT. Thus, the parent phenotype is enriched in their respective mTDT, but the instability of mTDT immune infiltrate patterns suggest that variation in host biology, even in inbred mouse strains, mediates establishment of the immune contexture. This aspect of mTDT may be useful for identifying host mechanisms that increase response to immune checkpoint blockade.

The limitations of the model include lack of HER2 amplification or hormone receptor positive mTDT that represent major human breast cancer subtypes. Spontaneous HER2 amplification is uncommon in mouse mammary cancers, although a few such *Trp53* null mammary tumors have been reported (21). This model does give rise to estrogen and progesterone positive cancers (19), but our random selection from stocks happened to have only one hormone receptor positive parent and the resulting mTDT did not maintain hormone receptors upon transplantation. Thus, the potential for generating ER positive mTDT remains to be thoroughly tested.

Nonetheless, several aspects of the model are potentially useful. First, the *Trp53* null mTDT contribute biological diversity in a range of serially transplantable mammary carcinomas in immunocompetent BALB/cJ mice, and provides a diverse model in which to simultaneously study the systemic host immunity and immune component of the TME. This overcomes a critical limitation of patient-derived xenografts that are by necessity established in immune-deficient mice (15). The TIL patterns of human cancers are associated with the likelihood of response to immunotherapy (2-4). Supervised hierarchical clustering of infiltrated tumors using 18-genes associated with T cell exhaustion suggest prolonged antigen stimulation of lymphocytes and loss of effector function. Human tumors with a brisk, active immune cell infiltrate are more responsive to immunotherapy, while those in which TIL are absent or excluded are not. One therapeutic goal is to convert the latter to active immune cell infiltrate by treatment. Having a syngeneic model that gives rise to the so-called cold tumors can be used to investigate different mechanisms of conversion, such as that proposed for radiotherapy (44).

Second, most of the primary and mTDT tumors were ER and PR-negative, of which the majority were infiltrated. TNBC have the highest frequency of tumor infiltrating CD8+ lymphocytes, but regardless of ER status, the presence of TIL correlates with a good prognosis (45). Using intrinsic TNBC subtyping gene signatures, we determined the molecular profiles of mTDT are distributed similarly compared with human breast cancer, in that most mTDT classify as mesenchymal, mesenchymal stem-like or immunomodulatory. The mesenchymal and mesenchymal stem-like, are heavily enriched in pathways related to cell motility, cell differentiation, Wnt and TGFβ signaling, and angiogenesis. Most of the desert and excluded mTDT subtyped as mesenchymal, while 50% of infiltrated tumors were immunomodulatory. Immunomodulatory gene ontologies are enriched in immune cell processes and immune signal transduction including cytokine signaling, antigen processing, and presentation and the complement cascade. Interestingly, excluded and desert tumors were subtyped as either basal-like 1 or 2 or mesenchymal, which are characterized by increased proliferation, elevated expression of DNA damage response genes, cellular differentiation, TGFβ signaling, and angiogenesis, consistent with the gene expression analysis. Mariathasan et al. showed lack of response to anti-PD-L1 agent was associated with TGFβ signaling in fibroblasts leading to exclusion of CD8+ T cells from the tumor and low tumor mutational burden (34).

Third, TNBC patients have a high risk of metastasis to the lung, bone and liver. We found that some mTDT have metastatic potential that appears to be associated with family origin and not TIL phenotype since metastatic spread was observed in mTDT of desert, infiltrated and excluded families. Notably, all mTDT from infiltrated family K, which has a poorly differentiated histology and a basal-like breast intrinsic molecular subtype, metastasized, providing a new model to investigate TNBC metastasis.

Fourth, at the transcriptomic level, immune related genes were transcriptionally similar from mTDT generation to generation. The lack of gene expression divergence across generations suggests that those genes and the processes they modulate are intrinsically coordinated. A critical component may be TGFβ, whose activity was both evident in terms of signaling and transcriptional targets. Desert tumors are described as immunologically ignorant tumors that rarely express PD-L1 and are associated with high proliferation, low mutational burden and low expression of antigen presentation markers such as major histocompatibility complex (MHC) class I (3). Primary tumors and mTDT with the desert phenotype were grouped by expression of genes that invoke pathways including proliferation and DNA damage response. The programs implied among infiltrate phenotypes by this abbreviated analysis warrant further exploration with single-cell RNA sequencing.

This newly established breast cancer model in a syngeneic immunocompetent mouse recapitulates the heterogeneity, molecular features, diverse TIL patterns and response to immunotherapy observed in humans. Elucidation of the intrinsic molecular features and TME composition effects on cytotoxic T cell activity is critical to further evolution of therapeutic strategies. Interestingly, comparison of the TME of mTDT grown subcutaneously or orthotopically suggests that composition is not uniformly affected by location. Only a subset of TNBC patients in the metastatic and neoadjuvant settings and a subset of hormone-receptor positive patients in the neoadjuvant setting respond to immune checkpoint inhibitors (46-48). Based on the presence of TIL in mTDT from infiltrated families, we expected mTDT to respond to single agent anti-PD-L1 immunotherapy. However, there was no objective response measured by growth rate or survival of either orthotopic or subcutaneous mTDT from 6 parental origins, despite the presence of PD-L1 and CD8+ T cells. Gene expression data suggest that the lymphocytes of infiltrated tumors are activated but ineffective; we speculate that the nearly 1:1 correspondence between CD8+ T cells and F4/90 macrophages density may be a factor.

Although the immune TME is a critical barrier to effective therapy, there is growing recognition that systemic anti-tumor immunity is major determinant of response to immunotherapy (49). Analysis of both TME and peripheral immunity can be explored in this model to further evaluate the requisite biology of effective immunotherapy. This initial collection of 12 syngeneic mTDT that recapitulate complex patterns of immune escape is a much-needed resource to evaluate response to treatment regimens and a robust model to discover mechanisms by which tumor cells evade the immune system.

Acknowledgements

The authors would like to thank Dixon F Hoffelt, Trevor Jones and William Chou for technical support. This research was supported by the imCORE Network, project USC-3, on behalf of Genentech Inc. and by NIH R01CA190980 and R01CA239235 awards to MHBH. JM was supported by NIH R01CA190980S1 and under Award Number T32CA108462. Tissue processing and immunostaining was performed using the Helen Diller Family Comprehensive Cancer Center Pathology Shared Resource, supported by the National Cancer Institute of the National Institutes of Health under Award Number P30CA082103. The content is solely the responsibility of the authors and does not necessarily represent the official views of the National Institutes of Health.

REFERENCES

1. DeNardo DG, Coussens LM. Inflammation and breast cancer. Balancing immune response: crosstalk between adaptive and innate immune cells during breast cancer progression. Breast cancer research : BCR **2007**;9:212
2. Salgado R, Denkert C, Demaria S, Sirtaine N, Klauschen F, Pruneri G*, et al.* Harmonization of the evaluation of tumor infiltrating lymphocytes (TILs) in breast cancer: recommendations by an international TILs-working group 2014. Annals of oncology : official journal of the European Society for Medical Oncology / ESMO **2014**
3. Hegde PS, Karanikas V, Evers S. The Where, the When, and the How of Immune Monitoring for Cancer Immunotherapies in the Era of Checkpoint Inhibition. Clin Cancer Res **2016**;22:1865-74
4. Loi S, Drubay D, Adams S, Pruneri G, Francis PA, Lacroix-Triki M*, et al.* Tumor-Infiltrating Lymphocytes and Prognosis: A Pooled Individual Patient Analysis of Early-Stage Triple-Negative Breast Cancers. Journal of clinical oncology : official journal of the American Society of Clinical Oncology **2019**;37:559-69
5. Loi S, Drubay D, Adams S, Francis PA, Joensuu H, Dieci MV*, et al.* Pooled individual patient data analysis of stromal tumor infiltrating lymphocytes in primary triple negative breast cancer treated with anthracycline-based chemotherapy. Cancer research **2016**;76
6. Denkert C, von Minckwitz G, Darb-Esfahani S, Lederer B, Heppner BI, Weber KE*, et al.* Tumour-infiltrating lymphocytes and prognosis in different subtypes of breast cancer: a pooled analysis of 3771 patients treated with neoadjuvant therapy. The Lancet Oncology **2018**;19:40-50
7. Bindea G, Mlecnik B, Angell HK, Galon J. The immune landscape of human tumors: Implications for cancer immunotherapy. Oncoimmunology **2014** 3:e27456
8. Dirix LY, Takacs I, Jerusalem G, Nikolinakos P, Arkenau HT, Forero-Torres A*, et al.* Avelumab, an anti-PD-L1 antibody, in patients with locally advanced or metastatic breast cancer: a phase 1b JAVELIN Solid Tumor study. Breast cancer research and treatment **2018**;167:671-86
9. Adams S, Schmid P, Rugo HS, Winer EP, Loirat D, Awada A*, et al.* Pembrolizumab monotherapy for previously treated metastatic triple-negative breast cancer: cohort A of the phase II KEYNOTE-086 study. Annals of oncology : official journal of the European Society for Medical Oncology / ESMO **2019**;30:397-404
10. Emens LA, Cruz C, Eder JP, Braiteh F, Chung C, Tolaney SM*, et al.* Long-term Clinical Outcomes and Biomarker Analyses of Atezolizumab Therapy for Patients With Metastatic Triple-Negative Breast Cancer: A Phase 1 Study. JAMA oncology **2019**;5:74-82
11. Amundson SA, Do KT, Vinikoor LC, Lee RA, Koch-Paiz CA, Ahn J*, et al.* Integrating global gene expression and radiation survival parameters across the 60 cell lines of the National Cancer Institute Anticancer Drug Screen. Cancer research **2008**;68:415-24
12. Kopetz S, Lemos R, Powis G. The promise of patient-derived xenografts: the best laid plans of mice and men. Clin Cancer Res **2012**;18:5160-2
13. Langdon SP, Hendriks HR, Braakhuis BJ, Pratesi G, Berger DP, Fodstad O*, et al.* Preclinical phase II studies in human tumor xenografts: a European multicenter follow-up study. Annals of oncology : official journal of the European Society for Medical Oncology / ESMO **1994**;5:415-22
14. Aparicio S, Hidalgo M, Kung AL. Examining the utility of patient-derived xenograft mouse models. Nat Rev Cancer **2015**;15:311-6
15. Dobrolecki LE, Airhart SD, Alferez DG, Aparicio S, Behbod F, Bentires-Alj M*, et al.* Patient-derived xenograft (PDX) models in basic and translational breast cancer research. Cancer Metastasis Rev **2016**;35:547-73

16. Borowsky AD. Choosing a mouse model: experimental biology in context--the utility and limitations of mouse models of breast cancer. Cold Spring Harbor perspectives in biology **2011**;3:a009670
17. Jerry DJ, Kittrell FS, Kuperwasser C, Laucirica R, Dickinson ES, Bonilla PJ*, et al.* A mammary-specific model demonstrates the role of the p53 tumor suppressor gene in tumor development. Oncogene **2000**;19:1052-8
18. Medina D, Ullrich R, Meyn R, Wiseman R, Donehower L. Environmental carcinogens and p53 tumor-suppressor gene interactions in a transgenic mouse model for mammary carcinogenesis. Environ Mol Mutagen **2002**;39:178-83
19. Nguyen DH, Oketch-Rabah HA, Illa-Bochaca I, Geyer FC, Reis-Filho JS, Mao JH*, et al.* Radiation Acts on the Microenvironment to Affect Breast Carcinogenesis by Distinct Mechanisms that Decrease Cancer Latency and Affect Tumor Type. Cancer Cell **2011**;19:640-51
20. Nguyen DH, Ouyang H, Mao JH, Hlatky L, Barcellos-Hoff MH. Distinct luminal type mammary carcinomas arise from orthotopic Trp53 null mammary transplantation of juvenile versus adult mice. Cancer research **2014**;74:7149-58
21. Herschkowitz JI, Zhao W, Zhang M, Usary J, Murrow G, Edwards D*, et al.* Comparative oncogenomics identifies breast tumors enriched in functional tumor-initiating cells. Proceedings of the National Academy of Sciences **2011**;109:2778-83
22. Nguyen DH, Fredlund E, Zhao W, Perou CM, Balmain A, Mao J-H*, et al.* Murine Microenvironment Metaprofiles Associate with Human Cancer Etiology and Intrinsic Subtypes. Clin Cancer Research **2013**;19:1353-62
23. Omene C, Ma L, Moore J, Ouyang H, Illa-Bochaca I, Chou W*, et al.* Aggressive Mammary Cancers Lacking Lymphocytic Infiltration Arise in Irradiated Mice and Can Be Prevented by Dietary Intervention. Cancer immunology research **2020**;8:217-29
24. Illa-Bochaca I, Ouyang H, Tang J, Sebastiano C, Mao J-H, Costes SV*, et al.* Densely Ionizing Radiation Acts via the Microenvironment to Promote Aggressive Trp53 Null Mammary Carcinomas. Cancer research **2014**;74:7137-48
25. Tang J, Fernandez-Garcia I, Vijayakumar S, Martinez-Ruiz H, Illa-Bochaca I, Nguyen DH*, et al.* Irradiation of juvenile, but not adult, mammary gland increases stem cell self-renewal and estrogen receptor negative tumors. Stem Cells **2013**;32:649-61
26. Parra ER, Uraoka N, Jiang M, Cook P, Gibbons D, Forget M-A*, et al.* Validation of multiplex immunofluorescence panels using multispectral microscopy for immune-profiling of formalin-fixed and paraffin-embedded human tumor tissues. Scientific reports **2017**;7:13380
27. Liu Q, Ma L, Jones T, Palomero L, Pujana MA, Martinez-Ruiz H*, et al.* Subjugation of TGFb Signaling by Human Papilloma Virus in Head and Neck Squamous Cell Carcinoma Shifts DNA Repair from Homologous Recombination to Alternative End Joining. Clin Cancer Res **2018**;24:6001-14
28. Liao Y, Smyth GK, Shi W. The R package Rsubread is easier, faster, cheaper and better for alignment and quantification of RNA sequencing reads. Nucleic acids research **2019**;47:e47-e
29. Laird NM, Ware JH. Random-Effects Models for Longitudinal Data. Biometrics **1982**;38:963-74
30. Chen DS, Mellman I. Elements of cancer immunity and the cancer-immune set point. Nature **2017**;541:321-30
31. Lee SH, Kim Y-S, Han W, Ryu HS, Chang JM, Cho N*, et al.* Tumor growth rate of invasive breast cancers during wait times for surgery assessed by ultrasonography. Medicine **2016**;95:e4874

32. Cristescu R, Mogg R, Ayers M, Albright A, Murphy E, Yearley J*, et al.* Pan-tumor genomic biomarkers for PD-1 checkpoint blockade–based immunotherapy. Science (New York, NY) **2018**;362:eaar3593
33. Hugo W, Zaretsky JM, Sun L, Song C, Moreno BH, Hu-Lieskovan S*, et al.* Genomic and Transcriptomic Features of Response to Anti-PD-1 Therapy in Metastatic Melanoma. Cell **2016**;165:35-44
34. Mariathasan S, Turley SJ, Nickles D, Castiglioni A, Yuen K, Wang Y*, et al.* TGFbeta attenuates tumour response to PD-L1 blockade by contributing to exclusion of T cells. Nature **2018**;554:544-8
35. Quaranta V, Schmid MC. Macrophage-Mediated Subversion of Anti-Tumour Immunity. Cells **2019**;8:747
36. Burstein MD, Tsimelzon A, Poage GM, Covington KR, Contreras A, Fuqua S*, et al.* Comprehensive Genomic Analysis Identifies Novel Subtypes and Targets of Triple-negative Breast Cancer. Clin Cancer Res **2014**
37. Hicks C, Kumar R, Pannuti A, Backus K, Brown A, Monico J*, et al.* An Integrative Genomics Approach for Associating GWAS Information with Triple-Negative Breast Cancer. Cancer informatics **2013**;12:1-20
38. Chen X, Li J, Gray WH, Lehmann BD, Bauer JA, Shyr Y*, et al.* TNBCtype: A Subtyping Tool for Triple-Negative Breast Cancer. Cancer informatics **2012**;11:147-56
39. Lehmann BD, Bauer JA, Chen X, Sanders ME, Chakravarthy AB, Shyr Y*, et al.* Identification of human triple-negative breast cancer subtypes and preclinical models for selection of targeted therapies. J Clin Invest **2011**;121:2750-67
40. Lyons YA, Wu SY, Overwijk WW, Baggerly KA, Sood AK. Immune cell profiling in cancer: molecular approaches to cell-specific identification. NPJ precision oncology **2017**;1:26
41. Lindau D, Gielen P, Kroesen M, Wesseling P, Adema GJ. The immunosuppressive tumour network: myeloid-derived suppressor cells, regulatory T cells and natural killer T cells. Immunology **2013**;138:105-15
42. Gonzalez-Junca A, Driscoll KE, Pellicciotta I, Du S, Lo CH, Roy R*, et al.* Autocrine TGFbeta Is a Survival Factor for Monocytes and Drives Immunosuppressive Lineage Commitment. Cancer immunology research **2019**;7:306-20
43. Jiang Y, Li Y, Zhu B. T-cell exhaustion in the tumor microenvironment. Cell death & disease **2015**;6:e1792
44. Ye JC, Formenti SC. Integration of radiation and immunotherapy in breast cancer - Treatment implications. Breast **2018**;38:66-74
45. Sobral-Leite M, Salomon I, Opdam M, Kruger DT, Beelen KJ, van der Noort V*, et al.* Cancer-immune interactions in ER-positive breast cancers: PI3K pathway alterations and tumor-infiltrating lymphocytes. Breast Cancer Research **2019**;21:90
46. Nanda R, Liu MC, Yau C, Shatsky R, Pusztai L, Wallace A*, et al.* Effect of Pembrolizumab Plus Neoadjuvant Chemotherapy on Pathologic Complete Response in Women With Early-Stage Breast Cancer: An Analysis of the Ongoing Phase 2 Adaptively Randomized I-SPY2 Trial. JAMA oncology **2020**;6:676-84
47. Schmid P, Cortes J, Pusztai L, McArthur H, Kümmel S, Bergh J*, et al.* Pembrolizumab for Early Triple-Negative Breast Cancer. N Engl J Med **2020**;382:810-21
48. Schmid P, Adams S, Rugo HS, Schneeweiss A, Barrios CH, Iwata H*, et al.* Atezolizumab and Nab-Paclitaxel in Advanced Triple-Negative Breast Cancer. N Engl J Med **2018**;379:2108-21
49. Spitzer MH, Carmi Y, Reticker-Flynn NE, Kwek SS, Madhireddy D, Martins MM*, et al.* Systemic Immunity Is Required for Effective Cancer Immunotherapy. Cell **2017**;168:487-502.e15

FIGURES

Figure 1. Mammary tumor-derived transplant (mTDT) model.

A. Experimental scheme. F0 tumors were generated from *Trp53*-null mammary epithelium transplanted to cleared inguinal mammary glands (i.e., mammary chimera) and harvested as viably frozen fragments. F1 tumors were expanded in 8-week-old NCr nude mice and harvested as viably frozen fragments for further expansion as mTDT in BALB/cJ mice. **B.** Time to 10 mm^3 tumor for F2 (n=49, circle) and F3 (n=54, triangle) mTDT. *, *P*<0.05, Mann-Whitney test. Table showing the frequency of F3 mTDT implantation rate at subcutaneous (n=40) versus orthotopic (n= 40) from infiltrated F0 parents. **C.** Tumor growth rate over 30 days following detection of palpable tumor in each mouse. **D.** Representative histology (20X) for F0 parent compared to F1-F3 mTDT. Top panel, adenocarcinoma; middle panel, spindle cell; bottom panel, undifferentiated histology. Scale bars= 50 μm.

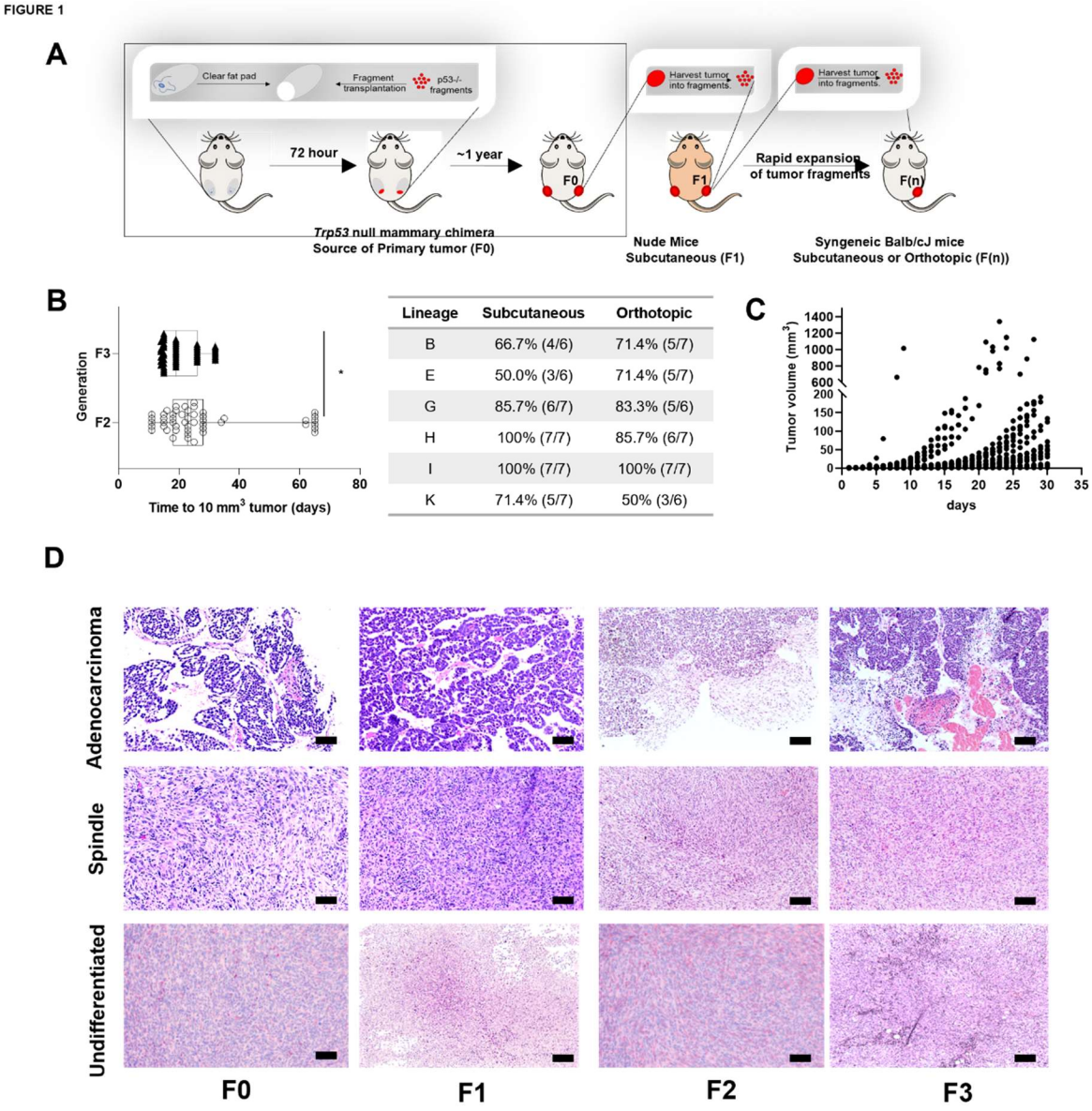

Lineage	Subcutaneous	Orthotopic
B	66.7% (4/6)	71.4% (5/7)
E	50.0% (3/6)	71.4% (5/7)
G	85.7% (6/7)	83.3% (5/6)
H	100% (7/7)	85.7% (6/7)
I	100% (7/7)	100% (7/7)
K	71.4% (5/7)	50% (3/6)

Figure 2. Assessment of mTDT TIL distribution and growth rates.
A. Experiment imaging scheme. **B**. Representative images of whole primary tumor sections stained with CD3 (red), CD8 (green), CD11b (yellow), CD45 (pink) and DAPI counterstained nuclei (blue) scanned by Vectra imaging system at 10X. White scale bars, 800 μm or 2 mm. Indicated TIL pattern was assigned based on qualitative assessment of CD8 distribution. **C.** Representative images of CD8+ T cells at tumor center (top) and edge (bottom). **D**. Average CD8+ T cells per 3-5 HPF at center (black) versus edge (gray) quantitatively defines infiltrated (n=31; dark green), excluded (n=17; blue) or desert (n=16; gold) phenotype. **E.** Ribbon plot of infiltrate phenotype fidelity of F2 and F3 tumors; infiltrated (dark green), excluded (blue) and desert (gold). Log-normal (LN) tumor growth rate of (**F**) F2 and (**G**) F3 mTDT for each lymphocyte infiltrate phenotype. *, *P*<0.05. The bars indicate the pointwise confidence interval.

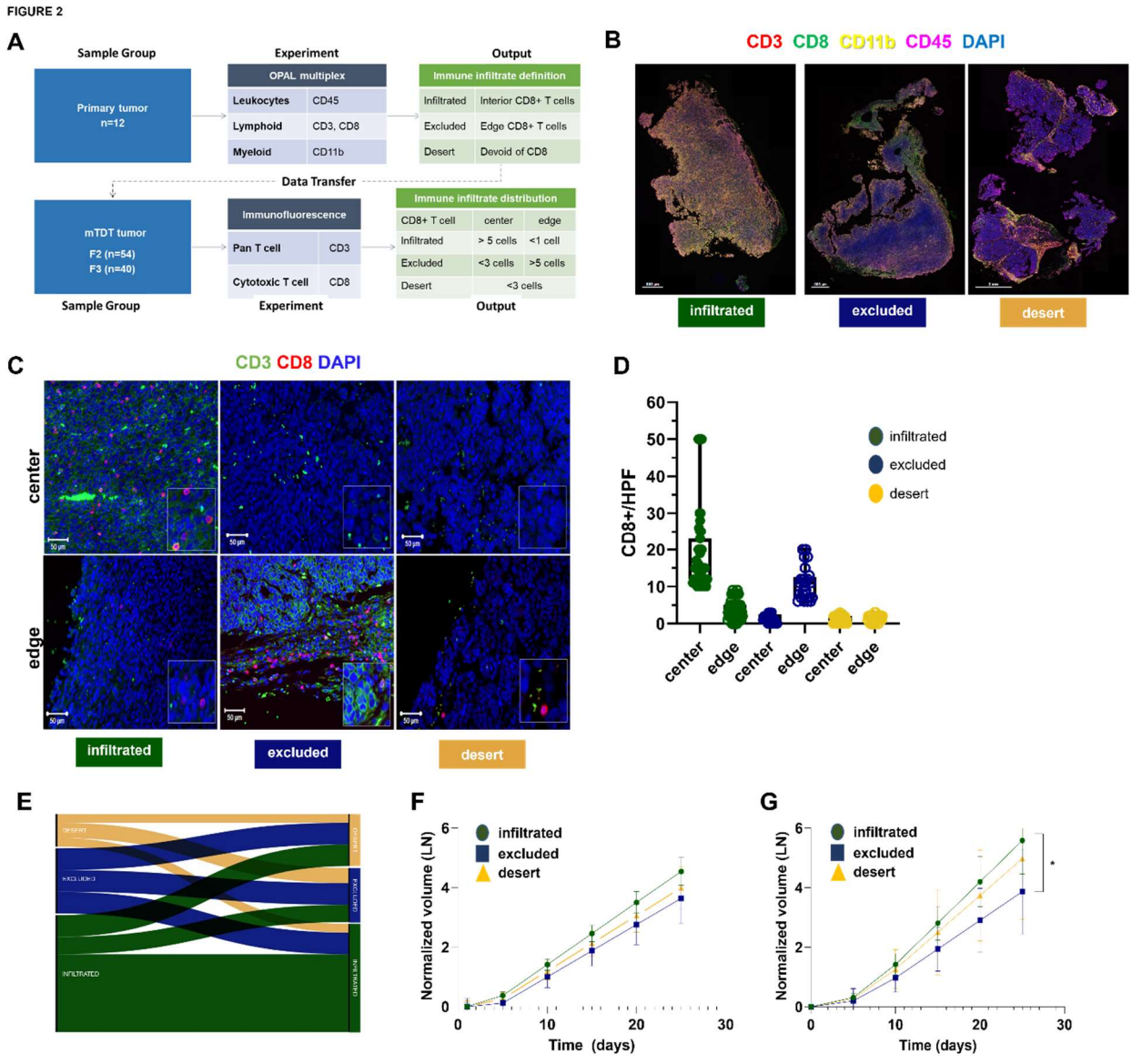

Figure 3. Comparison of orthotopic and subcutaneous mTDT response to anti-PD-L1.
A. Representative images of multiplex staining for CD8+ T cells (green), pSMAD2 (mauve), PD-L1 (red), F4-80 (yellow), pan-cytokeratin (white) and DAPI counterstained nuclei (blue) for parental tumors E, G, H, and I and corresponding orthotopic and subcutaneous mTDT. White scale bar, 20 μM. **B.** The percentage of stroma in orthotopic (orange circles) and subcutaneous (purple triangles) mTDT. ***, *P*<0.001. The cell density (number per mm^2) of (**C**) CD8, (**D**) PD-L1, (**E**) F4-80 and (**F**) pSMAD2 in mTDT from 4infiltrated parents grown in orthotopic (n=5, orange circles) versus subcutaneous (n=4, purple triangle) sites. **G.** Tumor growth curves of mTDT from 6 infiltrated families treated with anti-PD-L1 (purple) versus control antibody (black dash). **H.** Overall survival curve for mTDT from 6 infiltrated families treated with control IgG (black dash, n=27) or anti-PD-L1 (purple, n=31). **I.** Combined Kaplan-Meir survival graph of mTDT from family B (red), family E (green), G (pink), H (orange), I (blue) and K (gold). Cox regression analysis table of factors affecting survival of mTDT shown as Kaplan-Meir.

FIGURE 3

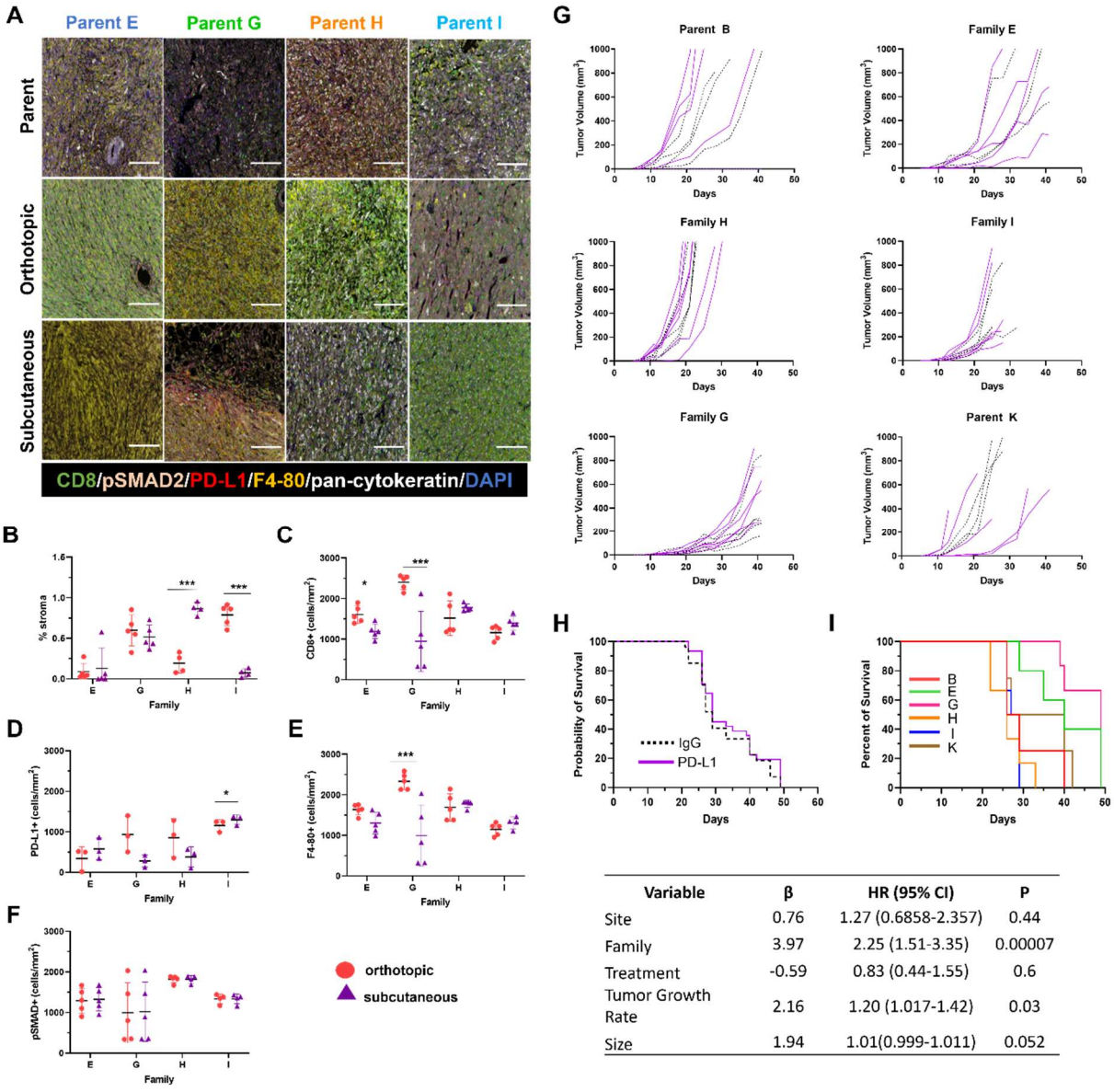

Variable	β	HR (95% CI)	P
Site	0.76	1.27 (0.6858-2.357)	0.44
Family	3.97	2.25 (1.51-3.35)	0.00007
Treatment	-0.59	0.83 (0.44-1.55)	0.6
Tumor Growth Rate	2.16	1.20 (1.017-1.42)	0.03
Size	1.94	1.01(0.999-1.011)	0.052

Figure 4. mTDT TIL phenotype-associated gene expression programs and intrinsic molecular profiles. **A.** Pie chart comparing generation F0 and F2 using PAM50 molecular subtyping: basal (pink), HER2 (orange), luminal (LUM) A (blue), LUM B (purple) and normal (gray). **B.** Pie chart comparing generation F0 and F2 using TNBCtype molecular subtypes: mesenchymal (green), immunomodulatory (blue), mesenchymal stem-like (purple), basal-like 1 and 2 (pink), luminal androgen receptor (orange) and unassigned (grey). **C.** Unsupervised hierarchical clustering of PanCancer IO360 gene expression of parental tumors (n=5, yellow) and F2 mTDT (n=19, black) analyzed by R software. Infiltrate: Infiltrated (dark green, n=13), excluded (blue, n=5), desert (gold, n=6)**.** Lineage: A (blue), B (mauve), C (black), D (grey), E (orange), F (light grey). Gene clusters 1-5 are indicated to right. Gene expression is scaled from high (blue) to low (yellow). . **D.** Unsupervised hierarchical clustering using ssGSEA of chronic TGFβ signature represented in the PanCancer IO360 panel. Legend described in **C. E.** Supervised hierarchical clustering of 18-genes associated with T cell exhaustion from PanCancer IO360 analysis of infiltrated B and F parent tumor (n=2, yellow) and F2 mTDT (n=11, black) analyzed by R software. Legends described in **C.** *, *P*<0.01 ***, *P*<0.001.

FIGURE 4